Editors' Suggestion

Enhancement of ice melting in isotropic turbulence

Aubrey L. McCutchan [1], Colin R. Meyer [2] and Blair A. Johnson [1,*]
[1] *Fariborz Maseeh Department of Civil, Architectural and Environmental Engineering, University of Texas at Austin, Austin, Texas 78712, USA*
[2] *Thayer School of Engineering, Dartmouth College, Hanover, New Hampshire 03755, USA*

(Received 10 February 2024; accepted 29 May 2024; published 2 July 2024)

Submarine melting at ice-ocean interfaces such as at tidewater glaciers and ice shelves is influenced by physical and chemical environmental factors including salinity, water temperature, stratification, subglacial hydrology, meltwater plumes, and oceanic currents. The effect of these individual components on ice loss can be difficult to capture in common ice-melting models. In particular, turbulence, which can develop as a result of ambient meltwater plumes and subglacial discharge along ice-water interfaces, for example, can increase mixing of relatively warm or high salinity ambient water with meltwater, thus enhancing melting. To isolate and understand the fundamental effects of turbulence on ice melting, we performed experiments of an ice sphere melting in homogeneous isotropic turbulence (HIT) with negligible mean flow. This setup permits us to study melting in turbulence absent additional fluid flows such as mean shear generated by boundary flows, or density stratification due to thermal or salinity gradients. To reduce the effects of complex ice morphology, we selected an ice sphere to achieve a symmetric melting surface. Ambient water temperature was varied from 2 to 10 °C. Experiments were performed with both quiescent and turbulent flow surrounding the ice. For the turbulent melting cases, the turbulent kinetic energy of the flow was varied from 9.6 to 28.6 $cm^2\,s^{-2}$. To link turbulence metrics and flow patterns to melting, we performed particle image velocimetry to obtain measurements of the two-dimensional velocity fields surrounding the sphere and to capture melting rates in experiments in a nonintrusive manner. Here, we explore the development of convective melt plumes and boundary layer flows that develop along the ice-water interface. We present melting data as a function of turbulence metrics and ambient water temperature. Through novel parametrization of our empirical results, our findings increase the understanding of the impact of turbulence on melting rates and aim to improve predictive numerical simulations of ice loss.

DOI: 10.1103/PhysRevFluids.9.074601

I. INTRODUCTION

Ice loss in the polar regions is accelerating [1,2], resulting in sea-level rise, increased storm surge, ocean encroachment of coastal areas, and altered oceanic and atmospheric circulations, among other effects [3]. Ocean-induced melting is a strong contributor to glacier mass loss. Melting at ice-ocean interfaces is influenced by salinity, stratification, oceanic currents, and subglacial plumes (among other environmental factors); this constitutes a large component of sea-level rise. Calving and submarine melting in Greenland alone are responsible for up to one-half of the total annual loss of ice into the ocean [4]. Accurate models of ice loss are essential to predict sea-level rise; however, recent studies have found common ice-melting models to underpredict ice melt [5,6].

*Contact author: blairjohnson@utexas.edu

Subglacial discharge plumes and ambient melt plumes are two flows that are prevalent at marine-terminating glaciers, yet remain difficult to accurately characterize [7]. Subglacial plumes originate from the subglacial hydrologic system, where meltwater originates from melt at the bottom of the glacier, groundwater, as well as inputs from the surface, such as moulins [8]. Subglacial plumes can carry significant sediment loads, affecting meltwater buoyancy [9]. By contrast, ambient melt plumes are formed along the submerged ice-water interface, where meltwater produced from instantaneous melting rises along the ice face. Ambient melt plumes and subglacial discharge plumes both originate from meltwater, thus they have low (or zero) salinity at their inception. As such, they are typically buoyant, as compared to saline ambient water. As both subglacial discharge plumes and ambient melt plumes rise along the ice-water interface, they generate shear at the plume-ice interface, as well as at the plume-ambient interface. This shear produces turbulence and subsequently promotes entrainment of ambient water into the plumes, causing the plume to become highly saline and/or to change temperature due to the proximity of the adjacent ambient water, in turn increasing ice loss as the plumes flow along the ice face [10,11].

At LeConte glacier in Alaska, Jackson *et al.* [5] found ambient melting (i.e., nondischarge driven melting) rates up to 100 times greater than predicted by models. At the same glacier, Sutherland *et al.* [6] observed total melting to be twice as fast as predicted and suggested melting models are not capturing complex feedback loops that influence melting rates. In particular, a common melting model called the *coupled plume-melt parametrization* uses turbulent transfer coefficients based upon empirical values that originated from studies on horizontal ice interfaces [12,13], but that have not been validated for near-vertical ice interfaces e.g., [14–17].

Collecting *in situ* measurements at glaciers in polar regions to improve ice-melting model parametrizations is difficult and costly. Furthermore, individual parameters of melting are challenging to study independently as melting at ice-ocean interfaces is affected by interconnected oceanic, glaciological, and atmospheric processes. However, individual parameters can be studied in idealized laboratory experiments. A variety of laboratory studies have been conducted to explore dominant mechanisms of ice melting and improve the accuracy of melting models (e.g., review by [18]). Prior studies have examined the dynamics of ice loss in both free and forced convective flows. These studies have incorporated ice geometries ranging from idealized scenarios to natural glaciers, and researchers have varied ambient water properties such as temperature, salinity, and stratification.

A. Literature review

Early ice-melting experiments focused on melting in free convection flows for geometries including ice spheres, horizontal ice sheets, and vertical ice faces, primarily using fresh water. Studies on ice spheres (e.g., [19–21]) used fresh water ranging in temperature from 1 to 25 °C to investigate heat transfer and boundary layer formation at the ice-water interface. Exploring effects surrounding the density anomaly of water using different ambient water temperatures, Schenk and Schenkels [20] and Vanier and Tien [21] both observed the formation of an upward flow of meltwater below 4 °C, dual flow between 4 and 6 °C, and downward flow at 6 °C and above. For vertical ice geometries in free convection flows, there were many studies that investigated ice melting in fresh water [22–26] and salt water [24,27–31], including salt water with an imposed density gradient [32–34]. Many of these studies also investigated flow patterns and boundary layer development at the ice face. Observations by Refs. [22,23,26,27] collectively suggested three flow regimes of the meltwater in their freshwater experiments, including upflow for ambient water temperatures below 4.4 °C, downflow above 7 °C, and the potential for dual or oscillatory flow for ambient water temperatures ranging from 4.4 °C to 7 °C, due to proximity to the 4 °C maximum density of water.

Beginning in the 2000s, the focus of many studies shifted to investigate ice melting in forced flows. For example, Hao and Tao [35] melted ice spheres in a horizontally driven flow, finding as water velocity and temperature were increased, the melting rate also increased. Subsequent studies with specific aims to better understand melting processes in the polar regions became more popular, with plumes and currents generated along vertical ice walls [36–39], ice blocks [40–42],

and horizontal ice sheets [43,44]. A limited number of studies considered ice melting in turbulence, including Machicoane *et al.* [45] who investigated the melting of secured ice spheres in (1) a turbulent swirling flow with zero mean velocity and (2) mean flow with low turbulence in fresh water. Machicoane *et al.* [45] used shadowgraphy to measure the size of the ice spheres; observations revealed heat transfer to be significantly more rapid with increased turbulence, given the faster melting observed in their data. Stapountzis *et al.* [46] melted ice spheres in quiescent water, in a facility designed to generate nearly isotropic and homogeneous turbulence with zero mean velocity using oscillating grids, and in an air facility using loudspeakers that generated synthetic jets. The ambient temperature in tests performed with water was 15 °C, while an ambient temperature of 23 °C was maintained in air tests. Observations included qualitative observations of convective boundary flows, where quantitative results showed as the turbulence intensity increased, the melting time significantly decreased, as a function of the sphere's hydraulic radius. A complementary body of literature has also developed regarding dissolution of substances (e.g., sugar spheres, salt blocks) in quiescent and moving fluids that provide insight on melting dynamics. While material properties and molecular diffusivity certainly play a key role in dissolution rates (analogous to thermal diffusivity), dissolution is also strongly enhanced by flows and stirring motions due to the disruption of boundary layers imposed by concentration (or thermal) gradients [47].

B. Goals and organization

The work presented herein investigates the fundamental melting dynamics of an ice sphere as a function of turbulence and ambient water temperature in idealized laboratory experiments. Specifically, we quantify melting in quiescent water and in zero mean flow homogeneous isotropic turbulence (HIT), which is statistically invariant of position and direction. The experimental apparatus used for this study to produce HIT (Sec. II) is inspired by previous apparatus that employed synthetic jets to produce HIT in air or water tanks (*inter alia*, [48–52]). Apparatus capable of producing zero mean flow HIT are valuable in fundamental studies as they reduce complexity in the parameter space while maintaining high energy levels and precise flow dynamics [53]. Additionally, numerical models that rely on untested empirical constants, such as those used for ice melting or mass transport, benefit from idealized laboratory studies that quantify the effect of turbulence or other flow conditions.

By producing HIT with zero mean flow, we seek to understand the underlying effect of turbulence on melting processes in water. For instance, environmental settings in polar regions may have some combination of density stratification, boundary layers, mean flows, and mean shear in addition to turbulence, whereas by using our customized turbulence-generating facility, we can isolate the effect of turbulence on melting. We complete an initial series of experiments to quantify melting of ice spheres in quiescent conditions at ambient water temperatures of 2, 4, 6, 8, and 10 °C to establish baseline melting rates in free convection, where buoyancy differences between meltwater and ambient water drive laminar flows. From these experiments, we report melt rates and boundary layer flow behavior of the meltwater plumes in Sec. III B. Next, we melt ice spheres in ambient water of temperatures 2, 4, 6, and 10 °C in HIT that is forced to produce energy values that match (and exceed) data obtained in coastal and polar sites. Melt rates and turbulence statistics are reported from these tests in Sec. III C.

II. EXPERIMENTAL FACILITY

A. Apparatus

Laboratory experiments were conducted in a turbulence-generating experimental tank in the Johnson Environmental Turbulence Laboratory (JETlab) at The University of Texas at Austin. The water tank has inner dimensions of 44.6 cm by 44.6 cm and a height of 50.35 cm, with acrylic walls that are 1.27 cm thick. Within the tank, there is a custom-made PVC frame that houses 20 Rule iL200 submersible inline pumps (3.3 gpm, 12V, 2.8 amp). The pumps are installed along the edges

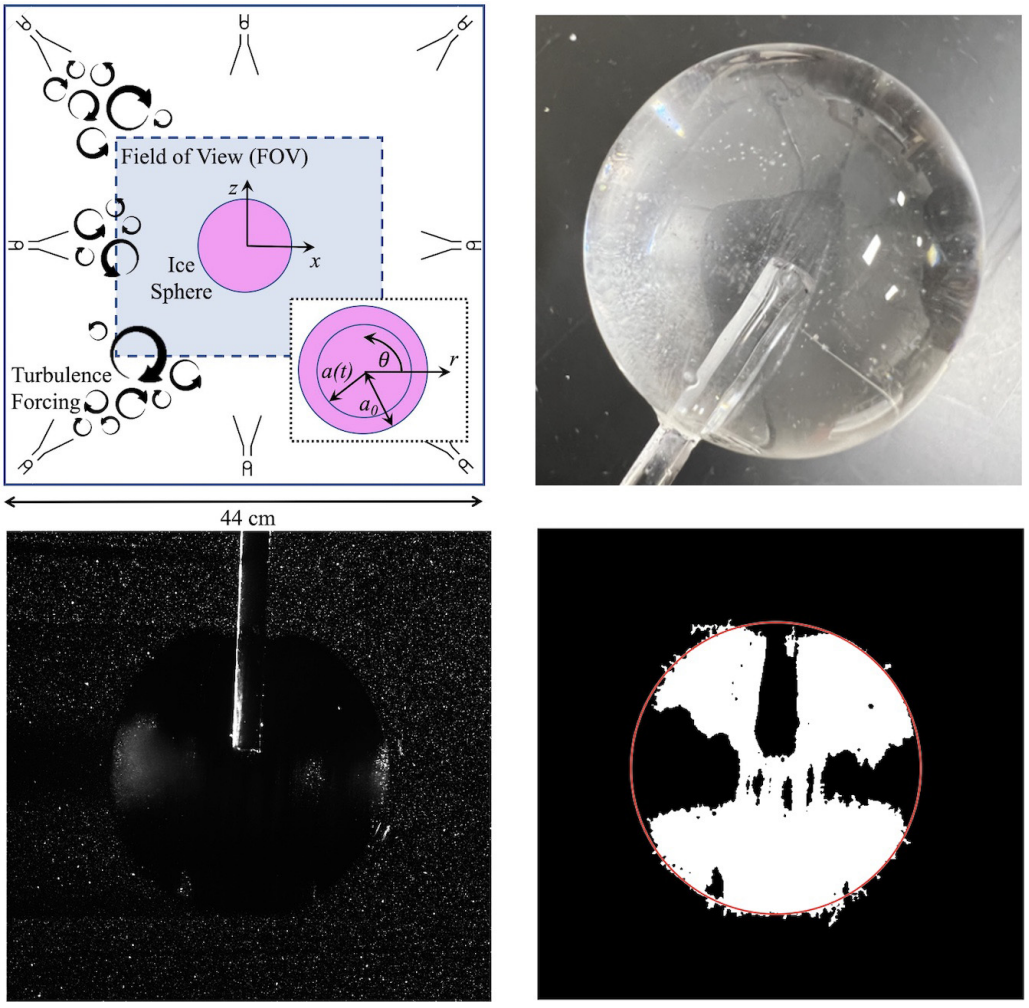

FIG. 1. Diagram of ice sphere centered within the experimental apparatus along with coordinate systems (upper left); photograph of the ice sphere (upper right); PIV image of the ice sphere (lower left) with circle identification for radius measurements (lower right).

and corners of the frame (Fig. 1). Custom-designed nozzles are mounted onto the pump outlets to direct the jets towards the center of the tank (via 90° and 45° elbows) and to sufficiently spread the momentum of each jet flow using a four-outlet nozzle for each pump for effective HIT generation. Further details about the facility are presented in McCutchan and Johnson [54]. Both Cartesian and spherical coordinate systems are used in the measurement plane, such that (x, z) and (r, θ) are both equal to (0,0) at the tank center. Radial distance from the center, r, is aligned with the positive, horizontally oriented x axis; z is oriented vertically, increasing upward; and θ is in the x-z plane (see Fig. 1). We note that y and φ, and statistics thereof, are neglected due to spherical symmetry and being outside of the measurement plane.

We use the "sunbathing" algorithm, developed by Variano and Cowen [55], to determine the pump operational states to minimize mean and secondary flows. Input algorithm parameters include mean on-time, T_{on}, mean off-time, T_{off}, and the instantaneous mean percentage of jet activity, on, where $\Phi_{\text{on}} = \frac{T_{\text{on}}}{T_{\text{on}}+T_{\text{off}}}$. The standard deviations for on-time and off-time, σ_{on} and σ_{off}, are selected as one-third of T_{on} and T_{off}, respectively [55]. Each pump is activated by custom-designed control

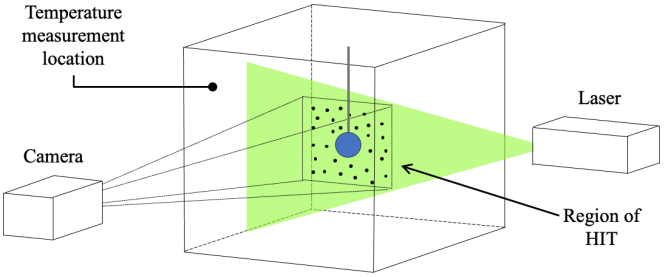

FIG. 2. Diagram of instrumentation for particle image velocimetry measurements within the turbulence facility.

boards fabricated by PJC Solutions, which are equipped with Texas Instruments SN74HC595N shift registers that receive on/off states from an Arduino Mega 2560 microcontroller, following Johnson and Cowen [56]. An AMETEK programmable power supply (model No. XG12-70MEB) provides power to the pumps, and pump voltage is selected by the user. Control of the voltage allows the pump outlet velocity, V_p, to be changed to customize generation of turbulence. A full characterization of the performance of this facility is presented in McCutchan and Johnson [54], highlighting the homogeneity and isotropy of the turbulence, while inducing negligible mean flows. For all turbulence tests performed herein, T_{on} was selected to be 1 s with $\Phi_{\text{on}} = 15\%$. Three different turbulence states were produced by varying jet velocity ($V_p = 185$, 217, 248 cm/s). In addition, a quiescent state was achieved when the jets were not operated ($\Phi_{\text{on}} = 0$).

Chilled tap water was added to the apparatus to achieve ambient water temperatures, T_w, of 2, 4, 6, 8, and 10 °C. Styrofoam insulation surrounded the tank exterior walls to maintain the water temperature, with openings to allow for optical instrumentation. A Fisherbrand Traceable digital thermometer (model No. 150778A) was used to record a point measurement of the water temperature before and after each ice-melting test. Temperature drift was approximately 0.1 °C per 10 min, increasing due to the room temperature. The majority of turbulence-enhanced melting tests were completed within 10 min, thus negligible temperature change was recorded. Separate tests confirmed heat generated by the jets had a negligible effect on the variation of the water temperature. For the melting tests with quiescent ambient water, tests were carried out for 20–37 min, resulting in ambient water temperature variations up to 0.3 °C.

The ice spheres used in the experiment were produced by freezing tap water in an insulated mold in which the water froze from the top down. This freezing method forces dissolved air to be pushed out as the water freezes, resulting in a nearly bubble-free ice sphere (see Fig. 1). We removed bubbles from the ice to reduce impacts on image quality from potential laser reflection effects. The ice spheres had an initial radius (a_0) of 2 cm. Each sphere contained a 0.3 cm by 0.3 cm square acrylic rod frozen 2 cm into the ice spheres, as shown in Fig. 1. The center of the acrylic rod was connected to a longer metal rod secured above the lateral center of the tank. The ice sphere was positioned such that its center coincided with the vertical, lateral, and horizontal center of the facility.

B. Measurement techniques

Velocity measurements in the center of the tank (coinciding with the center of the ice sphere; see Fig. 2) were collected using particle image velocimetry (PIV; [57]). The PIV data were used to measure the velocity of the meltwater plumes along with the convective currents that developed in cases of quiescent ambient water, and to characterize the HIT surrounding the ice sphere for the forced turbulent flow tests. The PIV images were also used to noninvasively measure the size of the sphere over time (Fig. 1). PIV provided two-dimensional, two-component velocities U and W, aligned with the x and z directions of the Cartesian coordinate system, respectively. The field of view (FOV), illuminated by an LRS-0532 DPSS laser from Laserglow Technologies, had a width of 14 cm

and height of 10 cm, encompassing the homogeneous and isotropic region found in McCutchan and Johnson [54] and surrounding the ice sphere. To capture image pairs for the cases with turbulent ambient flow, an Imperx CMOS camera (model PIV01882 from TSI Inc.) equipped with a Nikon Nikkor 50-mm lens (f/4) was used, operating at a sampling rate of 1 Hz. The time interval between images within a pair, ΔT, ranged from 5.5 to 6.5 ms for cases with forced ambient turbulence. For cases in which quiescent water surrounded the ice sphere, the convective flow velocities were relatively slow, driven by differences in density between the ambient water and the meltwater. To capture PIV images under these conditions, a continuous single-frame method was employed, with image capture rates contingent on the ambient water conditions. The time interval between each image within a pair, ΔT, varied between 250 and 330 ms to accurately measure the boundary layer dynamics of the meltwater plumes.

ORGASOL (R) 2002 ES 3 Nat 3 polyamide 12 nylon particles from Arkema Group with an average batch diameter (D_p) of 29.4 μm (8% greater than 40 μm and 5% less than 20 μm) and a specific gravity (S) of 1.03 were used to seed the tank for PIV measurements. The Stokes number, $\mathrm{St} = \tau_R/\tau_\mu$, which compares the particle relaxation time, $\tau_R = (S)D_p^2/18\nu$, where ν indicates the kinematic viscosity of water, to the Kolmogorov time scale, τ_μ, was found to be less than 0.01, indicating that these seeding particles behaved as passive tracers of the flow. Despite the particles not being frozen into the ice spheres, we were able to obtain velocity measurements near the ice-water interface due to the meltwater mixing with the seeded ambient water.

We used PIVlab [58,59] to analyze the PIV data. Analysis involved preprocessing images to enhance the contrast between the background and seeding particles to improve image quality. The selected subwindow sizes included 64 pixel by 64 pixel for two passes followed by 32 pixel by 32 pixel for two additional passes with 50% overlap, achieving a spatial resolution of 0.0036 cm/pixel and a vector-to-vector resolution of 0.058 cm for the final interrogation. Whereas vector fields were determined for the entirety of the FOV surrounding the ice sphere, only the right half of the FOV [recalling the center of the sphere is located at $(x, z) = (0, 0)$] was used for subsequent analyses, to remove any uncertainty caused by index-matching issues between the ice and ambient water. After applying an adaptive Gaussian window filter [60] and a spatial median filter to the velocity fields to remove high magnitude and other erroneous vectors [56], 98% valid data remained.

For the forced turbulence cases, Reynolds decomposition was used to investigate temporal variability of the flow, such that $U_i(x, y, z, t) = \langle U_i(x, y, z, t)\rangle + u_i(x, y, z, t)$, where U_i is the instantaneous velocity and u_i describes the velocity fluctuations. Temporally averaged values are denoted with angle brackets, whereas quantities that are both temporally and spatially averaged are denoted with an overbar. In the cases with turbulent forcing, flow metrics are presented in the far field, away from the influence of the ice sphere, where the flow remains homogeneous. The horizontal, lateral (perpendicular to the measurement plane), and vertical velocities are designated with $i = 1$, $i = 2$, and $i = 3$. These three components correlate to the directions of the x, y, and z axes, respectively.

We also used the PIV data to noninvasively measure the radius, $a(t)$, of the ice sphere during melting. A series of filters and custom MATLAB code was developed to process the raw PIV images to automate extraction of the change in the radius of the ice sphere over time, primarily leveraging the *imfindcircle* function in MATLAB. To improve circle identification by the algorithm, pre–processing steps included enhancing the contrast between the ice sphere and the ambient water. To accomplish this process, a mask was created by finding the maximum value for each pixel in 15 to 30 s intervals. This method made use of the seeding particles, which appear white in each image and have a high pixel intensity compared to the ice sphere pixel values, as the sphere appears black in the images. The time interval depended on the melting rate of the sphere as we wanted to minimize ice loss over each interval, but also capture enough seeding particles to provide sufficiently distinct contrast with the sphere. Additional steps involved smoothing the ice-water boundary of the sphere using a Gaussian filter, and binarizing the image to further optimize contrast between the sphere and the image background (Fig. 1). In preliminary testing, we used calipers to ensure that the ice remained spherical for the duration of testing, which subsequently allowed the use of a fully

noninvasive optical measure of sphere diameter over time for the melting tests performed herein. In other laboratory studies, melting rates were also determined by taking photographs of the ice as it evolved during the experiment (e.g., [30,39,45,46]) and measuring the change in the ice geometry.

III. RESULTS

We report ice-melting rates as a function of ambient water temperature and turbulence level. We first present findings of an analytical exercise that determines melt rates when melting is considered purely as a thermally driven process, neglecting buoyancy between meltwater and ambient water, in Sec. III A. In Sec. III B, we discuss melting rates and convective flows produced from our laboratory study of melting at the ice-water interface in initially quiescent conditions. In Sec. III C, we present melting rates in response to changes in ambient water temperature and to the imposed turbulent flow.

A. Analytical results of thermally driven melting in quiescent ambient water

As a starting point to understand the experimental results, we consider the axisymmetric melting of an isothermal ice sphere ($T = T_m$) in water that is held at a temperature above the melting point, $T_w > T_m$. Taking the fluid to be quiescent throughout and for the heat transfer in the fluid to be in steady state, the spherically symmetric solution to Laplace's equation that satisfies these conditions is

$$T = T_w - \frac{a\Delta T}{r}, \tag{1}$$

where $\Delta T = T_w - T_m$. Equation (1) shows that the temperature distribution in the fluid surrounding the ice sphere rises to the far-field value $T = T_w$ for $r \gg a$. The rate of melting is given by the Stefan condition, i.e.,

$$\rho_i \mathcal{L} \dot{a} = k_i \frac{\partial T_i}{\partial r} - k_w \frac{\partial T_w}{\partial r} \quad \text{at} \quad r = a, \tag{2}$$

where k_α are the thermal conductivities of ice and water, $\mathscr{L}$ is the latent heat, and ρ_i is the ice density. The melt rate is then given as

$$\dot{a} = -\frac{k_w \Delta T}{\rho_i \mathcal{L} a}. \tag{3}$$

Integrating, we can determine the radius a as a function of time, i.e.,

$$a = a_0 \sqrt{1 - \frac{2\kappa t}{a_0^2 \mathtt{St}} \frac{\rho_w}{\rho_i}}, \tag{4}$$

where a_0 is the initial sphere radius. We define the thermal diffusivity κ as $\kappa = k_w/(\rho_w c_p)$ where c_p is the specific heat. The Stefan number $\mathtt{St}$ is then

$$\mathtt{St} = \frac{\mathscr{L}}{c_p \Delta T}. \tag{5}$$

The Stefan number is typically moderately large for ice melting, for example, with $\Delta T = 8\,^\circ\mathrm{C}$, we have $\mathtt{St} = 10.4$. Based on Eq. (4), we see that the radius approaches zero at a time t_f, given by

$$t_f = \frac{a_0^2 \mathtt{St} \rho_i}{2\kappa \rho_w}. \tag{6}$$

At early times in Eq. (4), relative to t_f, we expect that the radius will decrease linearly as

$$a \approx a_0 \left(1 - \frac{\kappa t}{a_0^2 \mathtt{St}} \frac{\rho_w}{\rho_i}\right), \tag{7}$$

which is similar to what we observe in the experiments but, as we will show, a more rapid decrease in radius than predicted using a molecular value for thermal diffusivity κ.

If, however, we take the water heat flux in the Stefan condition to be linearly proportional to the temperature difference by a constant heat transfer coefficient h, as in

$$-k_w \frac{\partial T_w}{\partial r} \simeq -k_w h \Delta T, \tag{8}$$

then we find that the Stefan condition gives

$$\dot{a} = -\frac{k_w h \Delta T}{\rho_i \mathscr{L}}. \tag{9}$$

Integrating gives that the radius decreases linearly for all time, as

$$a = a_0 - \frac{\rho_w \kappa h}{\rho_i \mathrm{St}} t. \tag{10}$$

We can interpret our experimental results as a melting rate $M = -\dot{a}$, i.e., the decrease in sphere radius with time, da/dt. Equations (9) and (10) imply an empirical expression for the heat transfer coefficient h as a function of turbulence intensity and temperature difference.

B. Melting with quiescent ambient water

Given ambient water temperatures ranging from 2 to 10 °C, meltwater can be either positively or negatively buoyant. The density difference between the meltwater and ambient water results in the production of meltwater plumes that travel along the ice-water interface, ultimately producing upward or downward currents that detach from the sphere. The meltwater flows are also supported by convective currents of cooled ambient water in proximity to the ice. The initial ice temperature is −18 °C. We assume the meltwater temperature, T_m, to be equal to 0 °C at the moment of melting at the ice-water interface and warmer as it interacts with adjacent ambient water. Thus, in the studies for which T_w = 2,4,6 °C, we expect that the meltwater plume would initially be positively buoyant, given its relatively low density compared to that of the ambient water, and would subsequently rise through the tank. For the case of $T_w = 8$ °C, the density of the ambient water (0.999 849 g/cm^3) and the density of the 0 °C meltwater (0.999 841 g/cm^3) are almost matched, and so we expect the meltwater to remain near to its source at the ice-water interface given a lack of relative buoyancy, or for the meltwater to slowly rise given its slightly lower density than the 8 °C ambient water. Lastly, for $T_w = 10$ °C, the meltwater has a greater density than the ambient fluid, which we expect to result in a descending meltwater plume.

Indeed, for the cases in which $T_w = 2$ and 4 °C, upward-flowing meltwater plumes develop due to the density anomaly of water (i.e., the approximate 4 °C temperature of maximum density in water), as shown in Fig. 3. Also as expected, for $T_w = 10$ °C, we observed a downward-traveling meltwater plume, as depicted in Fig. 3. However, for $T_w = 8$ °C, our experimental observations reveal a consistently downward-flowing meltwater plume. We hypothesize that, although the meltwater temperature is equal to 0 °C at the instant of the phase change from solid to liquid, T_m rapidly increases due to its proximity to warmer ambient water and heat transfer across the boundary layer. In the case of $T_w = 8$ °C, only a slight temperature increase in T_m would be required for the meltwater plume to be of greater density than the ambient water. Additionally, any cooling of the 8 °C ambient water in proximity to the ice sphere would result in an increase in density of the ambient water, causing it to flow downward with the meltwater.

For the case in which $T_w = 6$ °C, intermittent and localized melting events strongly alter flow behavior, with instantaneous melt activity interrupting the development of a steady boundary layer. The density of water at 0 °C (recall, 0.999 841 g/cm^3) is less than the density of water at 6 °C (0.999 941 g/cm^3), leading us to expect an upward-flowing meltwater plume if we ignore conduction. Indeed, localized instantaneous upward-flowing meltwater events are observed sporadically

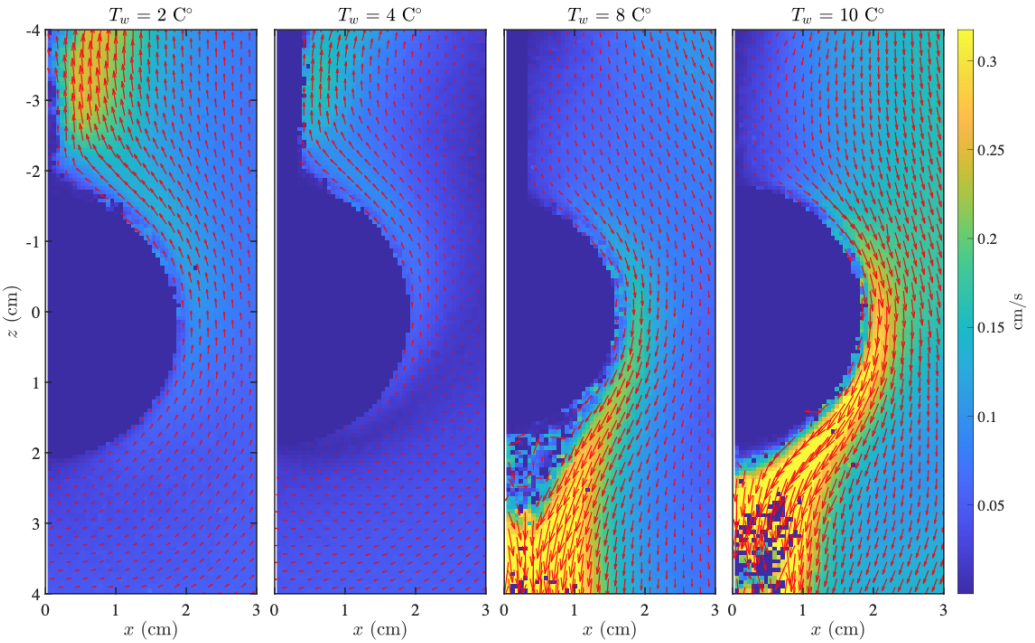

FIG. 3. Representative images of the developed boundary layer flows of the convective meltwater plumes at the ice-water interface in quiescent ambient water of $T_w = 2$, 4, 8, and 10 °C. Arrows indicate the direction and magnitude of velocity fields from the PIV data; the color bar indicates the velocity magnitude. Note several missing velocity vectors in the plume beneath the ice for $T_w = 8$ and 10 °C (indicated by zero magnitude) attributed to the absence of seeding particles in the ice, and thus missing PIV measurements in these locations.

during the tests (see, e.g., the upper-right region of the rightmost panel in Fig. 4). However, this upward-flowing meltwater does not generate a steady upward-flowing boundary layer as in the case of $T_w = 4$ °C. Instead, we notice dual flows, consistent with observations from the experiments of Refs. [20,22,23,26,27], which were conducted in fresh water for similar ambient water temperatures. Similar to the case in which $T_w = 8$ °C, it is feasible to hypothesize that heat transfer occurs from the ambient water to the meltwater, subsequently increasing the density of the localized meltwater plumes. Therefore, if the increase in T_m exceeds approximately 2 °C due to conduction, a downward-flowing meltwater plume would form when $T_w = 6$ °C. Indeed, over the full duration of testing, the bulk boundary layer flow that develops in the proximity of the ice sphere is downward in nature, but it is frequently interrupted by the upward melt events.

For each of these trials, the meltwater plume has a brief initial acceleration period from the inception of the experiment, once melting initiates and convective flows form. The meltwater plume forms a boundary layer along the surface of the ice sphere, apparent in Fig. 3 as relatively high-flow regions, and more weakly apparent in Fig. 4 with downward-flowing velocity vectors along the ice-water interface. The boundary layer develops azimuthally along the surface, reminiscent of the Coanda effect [61], before ultimately detaching into an upward or downward current traveling away from the sphere, depending on T_w.

1. Boundary layer characterization

In Figs. 3 and 5, we see evidence of a nearly no-slip boundary condition for flows tangent to the ice-water interface. Although meltwater forms at this interface (i.e., we presume flow emanates approximately normal to the surface when melting), the underlying ice remains solid and we can assume a low-flux boundary condition for the meltwater plume. The magnitude of the

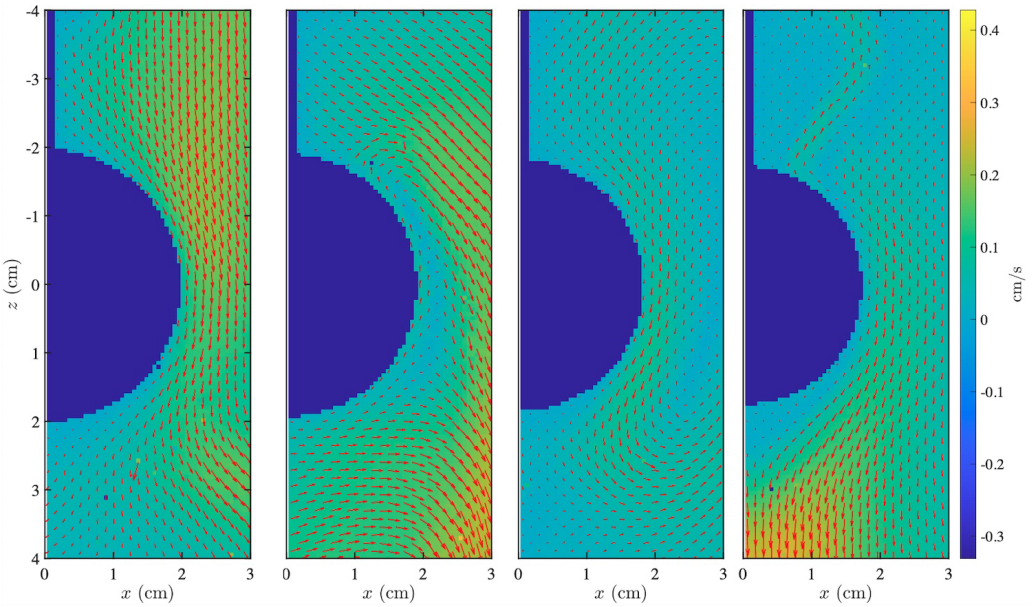

FIG. 4. Sample plots of the instantaneous velocity magnitude at the ice-water interface in quiescent ambient water of $T_w = 6\,^{\circ}\mathrm{C}$ showing intermittent local upward-flowing meltwater events [panels (b) and (d)] and dual flow behavior surrounding the ice sphere.

surface-parallel meltwater velocity first increases with radial distance from the edge of the sphere, up to some distance from the ice-water interface, due to gravitational (buoyancy) effects. Upon reaching a velocity maximum, the speed of the meltwater plume subsequently diminishes with distance from the sphere, due to drag imposed by the quiescent ambient water in the facility. With increasing distance from the ice-water interface, the presence of meltwater is relatively less beyond the location of the velocity peak; therefore, there is a reduction in buoyancy gradients to drive the flow.

To characterize the boundary layer flows, we consider radial profiles of velocity magnitude $U_m(r)$, where $U_m = \sqrt{U_1^2 + U_3^2}$, assuming $\langle U_2 \rangle \approx 0$. Because the boundary layer develops azimuthally (i.e., velocity increases with distance along the ice-water interface), we first look at velocity profiles along segments in 5° increments (see Fig. 5). Across the full duration of experiments for all T_w, the boundary layer appears to reach full development, just prior to detachment, at approximately $\theta = \pm 60^{\circ}$ (i.e., $\theta = +60^{\circ}$ for $T_w = 2$ and $4\,^{\circ}\mathrm{C}$, and $\theta = -60^{\circ}$ for $T_w = 6$, 8, and $10\,^{\circ}\mathrm{C}$). This angle of full development remains approximately steady for the duration of testing. Because the sphere radius diminishes as melting progresses, we define $r_a(t)$ as the radial distance from the ice-water interface [$r_a(t) = r - a(t)$] during melting. Similarly, we define a boundary layer thickness, δ_P, as the radial distance from the ice edge to the peak velocity; a schematic is provided in Fig. 6. We find the peak velocity magnitude increases nearly linearly with θ, an example of which is shown in Fig. 6. Here we see that while $U_{m,\max}$ develops linearly from $\theta = +60^{\circ}$ to $\theta = -40^{\circ}$ for an early case of melting at $10\,^{\circ}\mathrm{C}$, there is a departure from linearity beyond $\theta = -40^{\circ}$ due to plume detachment from the bottom of the sphere. By contrast, δ_P varies azimuthally, reaching a minimum near $\theta = 0^{\circ}$. Considering Figs. 3 and 4, it appears the meltwater flow (combined with convective currents from the ambient water) occupies a region roughly 0.5–1.0 cm from the ice-water interface (with $\delta_P \approx 0.2$–$0.6\,\mathrm{cm}$ across all tests).

Looking at the boundary layer profiles as they evolve in time [i.e., $U_m(r_a, t)|_{\theta=\pm 60^{\circ}}$; Fig. 7], we observe various behaviors, depending on T_w. For $T_w = 10\,^{\circ}\mathrm{C}$, there is an overall reduction in

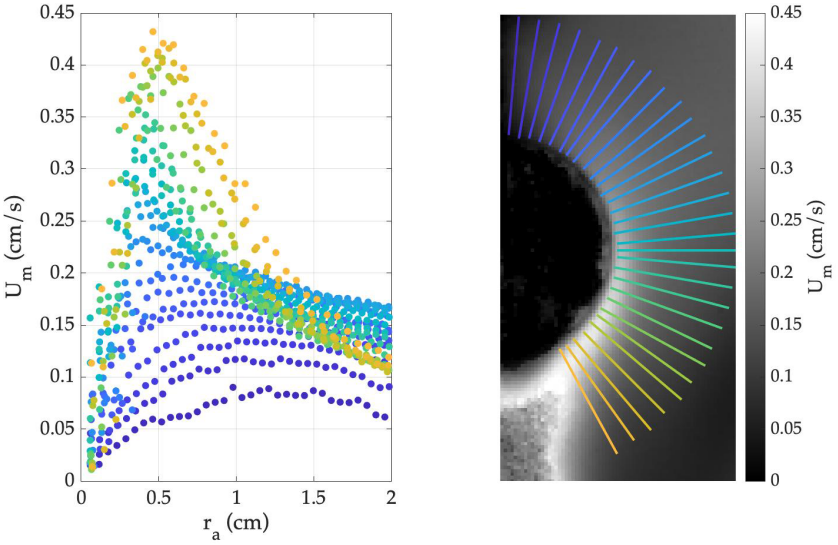

FIG. 5. Profiles of the velocity magnitude (left) outside of the sphere, located along radial segments spaced in 5° increments. Colors in the left plot of U_m correspond to colors overlaid on the velocity field (cm/s; right) for quiescent ambient water at $T_w = 10\,^{\circ}\mathrm{C}$ at $t = 2.5$ s.

peak velocity ($U_{m,\max}$) as melting progresses. For this case, there is a relatively rapid reduction in the available surface area of the ice with continued melting and weakening of the meltwater current. At the start of melting, the peak velocity promptly accelerates to 0.43 cm/s; it then reduces,

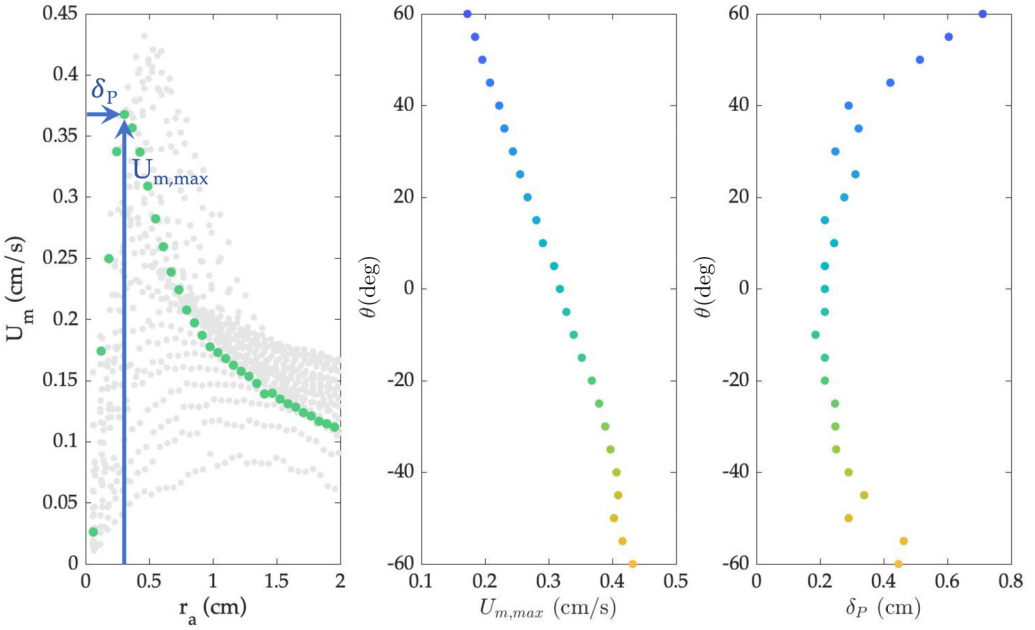

FIG. 6. Schematic of identifying the peak velocity magnitude and distance to peak velocity (i.e., boundary layer thickness; left) within the azimuthally developing melt plume velocity profiles; profile of peak velocity magnitude (center) and boundary layer thickness (right) as a function of azimuthal position (5° increments shown). Colors correspond with Fig. 5. Quiescent ambient water at $T_w = 10\,^{\circ}\mathrm{C}$ at $t = 2.5$ s.

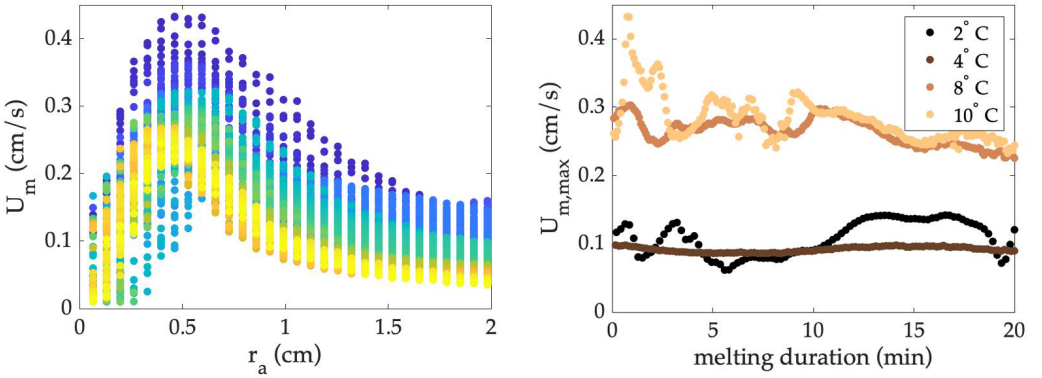

FIG. 7. Profiles of (left) boundary layer profiles U_m at $\theta = \pm 60^\circ$ for $T_w = 10\,^\circ$C. Time stack presented with dark blue indicating t_0 and light orange indicating $t = 20$ min. Temporal record of peak velocity at $\theta = \pm 60^\circ$ (right) for trials with stable boundary layer flows.

nonmonotonically, to approximately 0.25 cm/s. For other trials, however, the velocity is more stable, fluctuating only up to 0.05 cm/s for $T_w = 2$ and 8 °C without significant acceleration or deceleration, whereas $T_w = 4\,^\circ$C shows a nearly steady peak velocity.

To compare the meltwater boundary flows, we consider a boundary layer Reynolds number (Re_M), defined as

$$\mathrm{Re}_M = \frac{\rho_m U_{m,\max} C}{\mu_m}, \tag{11}$$

where ρ_m and μ_m are the density and dynamic viscosity of meltwater at 0 °C, $U_{m,\max}$ denotes the maximum meltwater speed within the sphere-attached plume immediately before detachment [i.e., at $\theta = \pm 60^\circ$], and C denotes half the circumferential length along the sphere at its central cross section at an initial diameter of 4 cm (i.e., $C = \pi a_0$, the maximum distance along which the plume could travel). Although $a(t)$ diminishes during melting and the meltwater plume detaches prior to $\theta = \pm 90^\circ$, and even though we believe the meltwater plumes exceed a temperature of 0 °C upon being warmed by ambient water, these assumptions provide a measure of the Reynolds number within an order of magnitude. To determine the maximum possible value of the meltwater Reynolds numbers ($\mathrm{Re}_{M,\max}$) across all quiescent ambient cases, we use the approximate maximum velocity observed across all tests, which occurred when $T_w = 10\,^\circ$C. Using a velocity $U_{m,\max}$ equal to 0.43 cm/s yields $\mathrm{Re}_{M,\max} = 150$, which is well within the range of laminar flow, and consistent with experimental observations of slow-moving smooth meltwater flows for the cases in which $T_w = 2$, 4, 8, and 10 °C. Whereas intermittent and unsteady flows certainly occur during melting for which $T_w = 6\,^\circ$C, these events do not appear to persist sufficiently to drive turbulence, as velocity magnitudes within the boundary layer region overall stay within ±0.22 cm/s. Peak values of $U_{m,\max}$ are presented in Table I.

2. Melting observations

Analysis of PIV images also provided the radius of the ice spheres as they diminished in time. Figure 8 reveals that the radius decays nearly linearly with time. Best-fit lines were applied to our data of $a(t)$, with R^2 values ranging from 0.87 to 0.99 across the five cases. We define melt rate as $M = da/dt$, given the observation of a linear recession of the sphere radius. We note that for our symmetric setup of a sphere, $M = da/dt$ is equivalent to approaches for mass-based melt quantification for objects of complex geometry (e.g., $M_W = \frac{dW}{\rho A dt}$, where dW is the mass lost to melting, A is the surface area of the ice, and dt refers to the duration of melting between measurements [41]). The values of our melt rate are summarized in Table I. As expected, warmer

TABLE I. Measured melt rates of ice spheres and convective velocity statistics of flow at the ice-water interface for quiescent ambient water. Velocity data presented for $U_{m,\max}$ at $\theta = \pm 60^\circ$.

T_w (°C)	M (cm/min)	$U_{m,\max}$ (cm/s)
2	0.004	0.14
4	0.014	0.10
6	0.019	0.22
8	0.040	0.30
10	0.062	0.43

ambient water temperatures resulted in faster melting. The finding that da/dt is linear is consistent with the early stages of melting in our analytical comparison (Sec. III A), along with the findings of several complementary studies, such as melt of a wax sphere in heated ambient liquid [62], and in the dissolution of solid caramel prisms in quiescent water, in spite of the development of irregular topography along the dissolution surface [63]. Interestingly, recent experiments of the dissolution of a solidified sugar (i.e., "hard candy" or "boiled sweets") sphere in initially quiescent water performed by Davies Wykes *et al.* [47] also showed nearly linear behavior of radius over time for the top half of the sphere; however, the sugar sphere did not remain spherical, exhibiting rapid dissolution in the bottom half of the sphere, likely due to the development of turbulence in the descending solute-laden jet beneath the sphere (as compared to our laminar plume that enabled consistent melting along the entire surface of the sphere). Similarly, laboratory experiments of eroding clay cylinders and melting ice spheres in channel flow have shown linear recession of the upstream faces and a linear recession of the downstream faces of the objects, with asymmetry due to the driven flow [35,64].

C. Turbulence-enhanced melting

We performed experiments in which the ambient flow was forced with three different turbulence levels (see Sec. II) at water temperatures of 2, 4, 6, and 10 °C. In these trials, meltwater was almost instantaneously mixed into the ambient water due to the energetic stirring from the turbulent forcing,

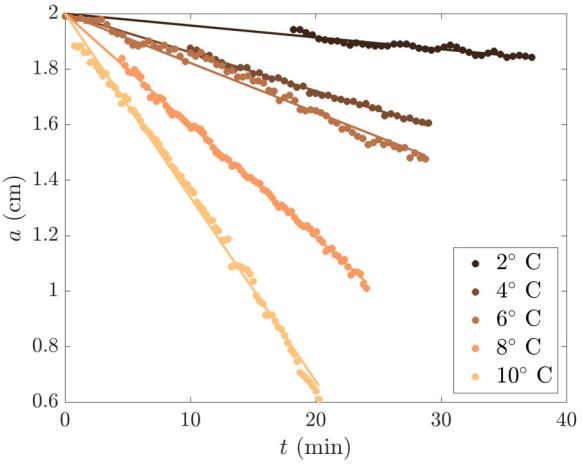

FIG. 8. Ice melt rates (raw data with best-fit lines) of the quiescent ambient cases, given as the radius of the ice sphere vs time.

TABLE II. The measured melt rate and turbulent kinetic energy of the flow for cases in which turbulence was generated around the ice sphere.

T_w (°C)	V_p (cm/s)	k (cm^2/s^2)	M (cm/min)
2	185	10.6	0.047
	217	18.1	0.052
	248	25.0	0.060
4	185	10.9	0.084
	217	17.4	0.099
	248	25.7	0.119
6	185	9.6	0.144
	217	15.7	0.194
	248	25.5	0.197
10	185	10.3	0.216
	217	16.8	0.257
	248	28.6	0.281

and there was no development of stable meltwater plumes, consistent with the notion that stirring reduces (or displaces) concentration boundary layers, thereby facilitating dissolution [65] or in this case, melting. Due to the symmetric and continuously forced turbulence, the ice remained spherical throughout the duration of testing.

First, we briefly quantify the far-field turbulence to which the sphere is subjected. To accomplish this, we compute a host of turbulence statistics in the 10 cm by 4 cm area outside of the influence of the ice sphere and to the right of the sphere. We then present melting observations in order to compare dynamics with convective flows and forced turbulence.

1. Turbulent flow characterization

The turbulent velocity fluctuations are characterized by the rms velocity, defined as $u_i' = \sqrt{\langle u_i^2 \rangle}$. The turbulent kinetic energy is calculated as $k = \frac{1}{2}(u_1'^2 + u_2'^2 + u_3'^2)$. From 2D PIV measurements, we obtain the $u_1'^2$ and $u_3'^2$ terms directly; however, $u_2'^2$ is estimated to be statistically equal to $u_1'^2$ given the symmetric facility design, such that $k = u_1'^2 + \frac{1}{2}u_3'^2$. As shown in Table II, the resulting values for k seem to be relatively unaffected by changes to T_w, despite minor changes to the water density and viscosity associated with the change in temperature. The turbulence facility was found to satisfy conditions of isotropy using the selected turbulence forcing parameters in McCutchan and Johnson [54]; we find that with the addition of the ice sphere, isotropy is maintained in the far field with ratios of $\frac{u_1'}{u_3'}$ ranging from 0.92 to 1.12 (with a target value of unity).

PIV data are used to determine the dissipation rate, $\epsilon \equiv 2\nu\langle S_{ij}S_{ij}\rangle$, where the strain rate S_{ij} is calculated as $S_{ij} \equiv \frac{1}{2}(\frac{\partial u_i}{\partial x_j} + \frac{\partial u_j}{\partial x_i})$. We assume radial symmetry about the z axis [54] and invoke continuity [60,66] such that ϵ can be computed directly as

$$\epsilon = 2\nu\left[4\overline{\left(\frac{\partial u_1}{\partial x_1}\right)^2} + \overline{\left(\frac{\partial u_1}{\partial x_3}\right)^2} + \overline{\left(\frac{\partial u_3}{\partial x_1}\right)^2} + 2\overline{\left(\frac{\partial u_3}{\partial x_3}\right)^2} + 2\overline{\left(\frac{\partial u_1}{\partial x_1}\frac{\partial u_3}{\partial x_3}\right)} + 2\overline{\left(\frac{\partial u_1}{\partial x_3}\frac{\partial u_3}{\partial x_1}\right)}\right]. \quad (12)$$

Upon calculating ϵ (see Table III), we determine the Kolmogorov length scale, $\eta \equiv (\nu^3/\epsilon)^{1/4}$, as a representative length scale of the smallest eddies of the flow. Across the three different turbulence conditions used, η ranges from 0.016 to 0.025 cm. This corresponds to the spatial resolution of PIV data ranging from 2.3 to 3.6η, indicating this resolution is sufficient to fully capture ($>99\%$) of the total dissipation via integration of the universal spectrum [67]. The Kolmogorov time

TABLE III. Turbulence statistics including the integral length scale, dissipation rate, Taylor scale Reynolds number, Taylor microscale, and Kolmogorov length and time scales for a combination of pump velocity values and ambient water temperatures. Turbulent statistics are reported as the spatial median of the time-averaged value within the isotropic region.

T_w (°C)	V_p (cm/s)	$\mathcal{L}_L$ (cm)	$\mathcal{L}_T$ (cm)	ϵ (cm^2/s^3)	Re$_\lambda$	λ (cm)	η (cm)	τ (s)
2	185	3.57	1.67	11.4	60	0.32	0.025	0.038
	217	3.23	1.84	20.3	80	0.30	0.022	0.029
	248	3.19	1.82	42.1	121	0.27	0.018	0.019
4	185	3.88	1.67	12.6	63	0.31	0.024	0.035
	217	3.84	1.97	20.0	80	0.31	0.021	0.028
	248	4.19	2.25	30.9	95	0.29	0.019	0.023
6	185	3.21	2.44	9.42	66	0.36	0.025	0.040
	217	2.91	1.71	19.6	75	0.28	0.020	0.027
	248	3.38	2.18	27.1	104	0.29	0.019	0.023
10	185	2.33	1.77	14.2	62	0.28	0.020	0.030
	217	2.78	1.80	19.5	86	0.27	0.019	0.026
	248	3.65	1.84	33.2	113	0.25	0.016	0.020

scale can also be approximated as $\tau \equiv (\nu/\epsilon)^{1/2}$. Values for turbulence statistics are reported in Table III.

The integral length scale describes the size of the largest eddies of the turbulent flow. We determine both longitudinal and transverse integral length scales, $\mathcal{L}_L$ and $\mathcal{L}_T$, respectively, from the autocorrelation functions ($A_{33,3}, A_{11,3}$) for the vertical and horizontal velocity data [56]. Whereas $\mathcal{L}_T$ is defined as $\int A_{11,3}(r)dr$, the longitudinal integral length scale is found using an exponential best-fit line to $A_{33,3}(r)dr$ as $A_{33,3}(r) = e^{-r/\mathcal{L}_L}$, following the methodology of Johnson and Cowen [56]. Values of $\mathcal{L}_L$ ranged from 2.33 to 4.19 cm, on the order of the initial ice sphere diameter, whereas $\mathcal{L}_T$ ranged from 1.67 to 2.44 cm. From our data we found the ratio of $\mathcal{L}_L/\mathcal{L}_T$ to range from 1.31 to 2.32 (with a target value of 2; [68]), suggesting near-isotropic turbulent flow. Following the determination of the integral length scales, the Taylor microscale (representative of the intermediate turbulent length scales) is calculated as $\lambda = \sqrt{10}\eta^{2/3}{\mathcal{L}_L}^{1/3}$, and ranges from 0.25 to 0.36 cm. The Taylor scale Reynolds number can subsequently be calculated as $\mathrm{Re}_\lambda = (\frac{2}{3}k)\sqrt{\frac{15}{\nu\epsilon}}$ and ranges from 60 to 121 across our experiments.

The turbulence within our facility matches and exceeds the energy measured at field sites of interest. The turbulent kinetic energy generated in our tests ranged from 9.6 to 28.6 cm^2/s^2. While near-ice turbulence measurements are difficult to obtain in the field, we can use measurements from other field sites to infer comparable turbulent kinetic energy level values for polar near-ice locations. For example, Talke *et al.* [69] obtained PIV measurements of upwelling water "boils" in a tidal river along the coast near Seattle, Washington. Results showed turbulent kinetic energy to range from 15 to 30 cm^2/s^2 in the vertical water column, consistent with our values. A limited number of dissipation measurements have been obtained in the Arctic Ocean and range from values of 10^{-7} to 1 cm^2/s^3 [70–74]; our measurements are much higher in our forced turbulent flow.

2. Melting observations

Similarly to the quiescent melt cases, the radius of the ice spheres decreased linearly with time when the ice was subjected to HIT, as shown in Fig. 9. In these tests, meltwater was rapidly stirred into the ambient water by the energetic turbulence. Therefore, the convective-driven boundary layers that developed in the quiescent cases were unable to form. This means the ice surface was almost

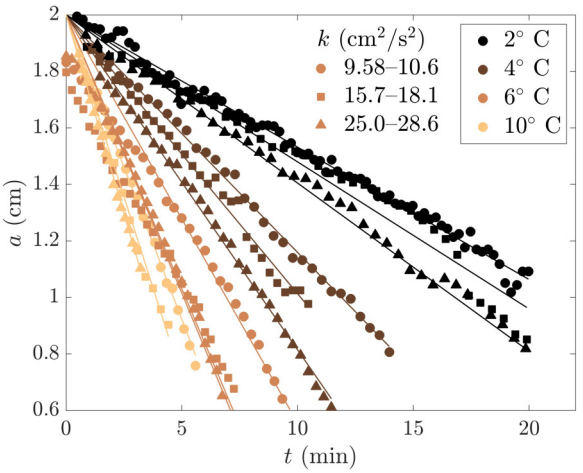

FIG. 9. Melting of ice in turbulent flow given as the radius of the ice sphere over time, with best-fit lines.

constantly exposed to the ambient water (and, analogously, to a source of heat), rather than having any instantaneous or localized insulation due to the presence of meltwater plumes. The linear behavior of sphere radius aligns well with the constant recession (or dissolution) of the faces of neutrally buoyant sugar particles studied by Oehmke and Variano [75] as they dissolved in isotropic turbulence, and following the model of constant mass flux from a dissolving surface [76].

Consistent with the findings of Machicoane *et al.* [45] and Stapountzis *et al.* [46], melting occurred more rapidly as turbulence levels increased, apparent in Fig. 9 and summarized in Table II. To investigate ice melting rates in turbulent flow, Stapountzis *et al.* [46] produced nearly isotropic and homogeneous turbulence with zero mean velocity where u' was varied from 3.4 to 5.8 cm/s with a constant ambient water temperature, $T_w = 15\,^\circ$C. While u' was similar in magnitude to our trials, their T_w was significantly higher than in our cases. Stapountzis *et al.* [46] presented melt rate as a function of the hydraulic diameter, D_H, versus time and obtained a nonlinear curve. In our trials, the ice spheres remained approximately spherical throughout the duration of melting, and so hydraulic diameter (i.e., $D_H = 4\frac{A}{P}$, where A is the surface area and P is the circumference of the ice) is equal to our sphere diameter, or $2a(t)$. The plot of hydraulic diameter versus time presented in Stapountzis *et al.* [46] shows slightly nonlinear behavior for a sphere melted fully, compared to our linear results for radius versus time for spheres melted to roughly half their initial diameter.

Looking at Fig. 10, we see that for either quiescent ambient water or forced turbulence, melt rate M increases nearly linearly with water temperature T_w. We fit a linear function with a zero y intercept as

$$M = \beta(T_w - T_m), \tag{13}$$

where β is the slope of the line and T_m is the water melting temperature ($0\,^\circ$C). We tabulate the values of β for the different turbulence levels in Table II. We perform the same analysis to explore the role of turbulence for fixed T_w, finding that for fixed T_w, the presence of turbulence facilitates melting, as compared to quiescent ambient. Further increases to k consequently increase M as well. However, as k increases, subsequent increases in the melting rate are reduced. In the rightmost panel of Fig. 10, square-root best-fit lines are plotted with the experimental data. From these fits, we propose a relationship by which melting increases with k such that

$$M \approx c_1 + c_2\sqrt{k} \tag{14}$$

with estimates of the temperature-dependent fit parameters presented in Table IV.

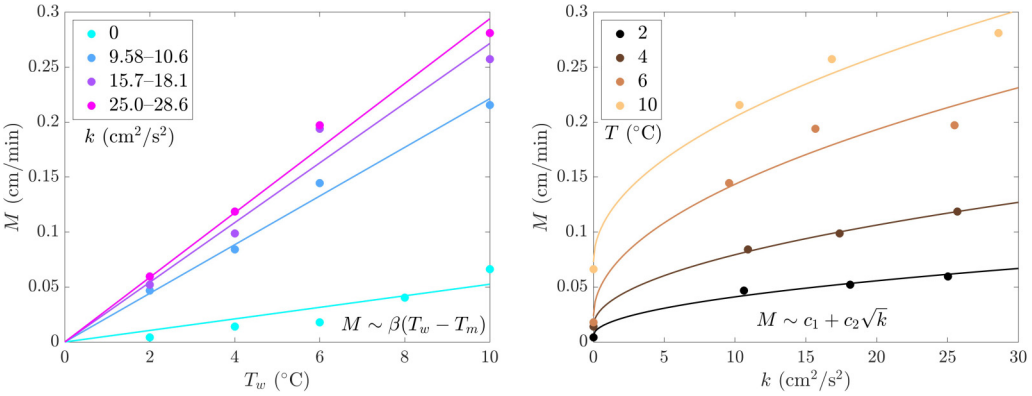

FIG. 10. Melt rate of the ice spheres as a function of ambient water temperature (left) for cases with quiescent and turbulent ambient with linear fits, and as a function of k for turbulent flow at $T_w = 2$, 4, 6, and 10 °C with square-root fits (right).

We note that an increase in the melt rate with $\sqrt{k}$ would be equivalent to an increase with u' in our zero mean flow isotropic turbulence experiments. Melting should also, by extension, occur more rapidly with an increase in the mean velocity of unidirectional turbulent flows, as in the forced plume experiments of Cenedese and Gatto [36], as velocity fluctuations scale with mean velocities in currents and plumes. In the experimental study of FitzMaurice *et al.* [40], which characterized melting of an ice block in channel flow, it was observed that at very low mean velocity the melt plumes remained attached to the ice, whereas at faster velocities the plumes detached, facilitating melting (by allowing warmer ambient water to reach the ice). In their study, conducted with salt water (32 ppt) at approximately 20 °C, only a slight increase in melt rate was measured for increasing flow velocity up to 2.5 cm/s. For flow velocities greater than 2.5 cm/s, the melt rate increased faster, maintaining a linear relationship. Our 10 °C quiescent melt experiment produced a melt rate of 0.062 cm/min, with a corresponding peak boundary layer velocity of 0.43 cm/s. If we assume $T_m = 0$ in Eq. (13), we calculate a rough estimate of M equal to 0.11 cm/min at 20 °C water, ignoring salinity. By comparison, FitzMaurice *et al.* [40] find a melt rate of approximately 0.13 cm/min corresponding to a forced mean flow velocity of 0.4 cm/s. For our turbulent melting cases at 10 °C, we see melt rates ranging from 0.216 to 0.281 cm/min, corresponding to values of $\sqrt{k}$ ranging from 3.2 to 5.3 cm/s. By comparison, mean flow velocities of 3.2 and 5.3 cm/s correspond to melt rates of roughly 0.18 and 0.28 cm/min in the FitzMaurice *et al.* [40]—experiments. Despite very different experimental setups—ours with either thermally driven laminar melt plumes or forced turbulence, and theirs with nearly laminar channel flow—we see similar values linking velocity data with melt rate. We note that vertical melt plume velocity was found to be in this range, at a magnitude of 4 cm/s, for simulations based on Sermilik Fjord in East Greenland [17], supporting the relevance of the selected velocity scales.

TABLE IV. Fit parameters for melting dependence on temperature (left) and on turbulence (right).

T_w (°C)	c_1 (cm/min)	c_2 (−)
2	0.0057	0.0112
4	0.0143	0.0206
6	0.0235	0.0379
10	0.0727	0.0418

V_p (cm/s)	β [cm/(min °C)]
0	0.0053
185	0.0221
217	0.0272
248	0.0294

Finally, we can relate expression (14) for the melt rate with the heat transfer coefficient h in Eqs. (9) and (10) to give

$$h = \frac{\rho_i \mathscr{L}(c_1 + c_2\sqrt{k})}{\rho_w c_p \kappa \Delta T}. \tag{15}$$

These empirical models for the melt rate and heat transfer coefficient as a function of turbulence intensity and temperature can be used as a starting point for investigating the role of turbulence on glacier ablation.

Jackson *et al.* [5] present detailed measurements at LeConte Glacier in Alaska, from which they estimate a melt rate of approximately 5 m/day (i.e., 0.35 cm/min) from their field campaign. They explore the variability in the turbulent transfer coefficients for heat and salinity [14,15] that would support such melt rates, finding that either the coefficients would need to be increased by an order of magnitude, and/or the ice face would need to be exposed to a horizontal mean velocity of up to 85 cm/s (compared to more likely estimates of 20 cm/s). Applying our fit parameters for Eq. (14) with their measured melt rate, using their measured water temperature minimum of approximately 6 °C (due to meltwater intrusions) and neglecting salinity, we estimate a corresponding magnitude of turbulent kinetic energy of 74 cm^2/s^2, or $\sqrt{k} = 8.6$ cm/s. Since there is a lack of velocity measurements in the immediate vicinity of glaciers, we perform a simplified calculation to compare our turbulence estimates with possible corresponding flows. In turbulent jets, for example, we estimate the ratio of $\sqrt{k}$ to mean velocity to range from roughly 14%–30% [68]; given our estimate of $\sqrt{k} = 8.6$ cm/s required to support melting of 5 m/day in 6 °C fresh water, a corresponding mean velocity may range from 26 to 60 cm/s. Although we do not yet have a way to characterize the independent or coupled roles of mean flow velocity and turbulence on melting, our estimates are well aligned with the measurements and estimates of Jackson *et al.* [5], and with prior laboratory experiments, despite being conducted at different physical scales and containing fewer melt-influencing mechanisms.

IV. CONCLUSIONS

We performed 17 experiments in which we melted an ice sphere in quiescent water at 2, 4, 6, 8, and 10 °C, then in turbulent flow in water at 2, 4, 6, and 10 °C where k was varied from 9.6 to 28.6 $\text{cm}^2\,\text{s}^{-2}$. In the quiescent melt cases, we collected PIV data to measure the velocity of the meltwater plumes that formed along the ice sphere. Analysis of boundary layer formation for each of the quiescent flow melting tests revealed an upflow for cases of $T_w = 2$ and 4 °C and downflow for cases of $T_w = 8$, and 10 °C. Dual flow was observed for $T_w = 6$ °C due to heat transfer into the melt plumes that caused initially rising meltwater to increase in density and become downflow. Because fresh water was used for all tests, buoyancy effects were present but small, with peak velocities with the meltwater plumes ranging from 0.14 to 0.43 cm/s. The PIV data were also used to extract the radius of the sphere over time in a noninvasive manner. The melt rate, defined as the change in sphere radius with respect to time, was linear for the duration of melting in all experiments with quiescent ambient, for the duration of testing. The melt rates for the quiescent cases were 0.004, 0.014, 0.019, 0.040, and 0.062 cm/min for $T_w = 2$, 4, 6, 8, and 10 °C, respectively. We found that the increase in melt rate was approximately linear with an increase in water temperature.

In the case of forced ambient homogeneous isotropic turbulence, PIV data were used to obtain flow statistics in the far field, including mean and turbulent velocities, turbulent kinetic energy, integral length scales, dissipation rates, Kolmogorov length and time scales, the Taylor scale Reynolds number, and the Taylor microscale. Due to the efficient stirring of the ambient turbulence (i.e., $\sqrt{k}$ from the forced turbulence cases is on the order of $10U_{m,\max}$ from the quiescent cases), localized melt plumes were promptly mixed into the surrounding water, preventing the formation of convective currents or steady boundary layer flows. Melting occurred faster in the turbulent cases as compared to quiescent cases. The approximately linear relationship between ambient water

temperature and melt rate was maintained for the cases with turbulent forcing. Individual melt rates for the 12 cases of melting in turbulent flow ranged from 0.047 to 0.281 cm/min. For the turbulence-induced melting, we found that for all ambient water temperature cases, the subsequent effect of k on melting decreased as k increased. The melt rate followed a square-root fit, where melting increased with $\sqrt{k}$. Extrapolating these results to existing field data on melting of LeConte Glacier, we see order of magnitude agreement with our findings and the estimates of associated flows and melt rates. While significant work remains to be performed to refine the links between thermal and fluid dynamics with melting, our findings offer a promising contribution to improving glacier melt predictions.

ACKNOWLEDGMENTS

We would like to thank Dr. Ginny Catania and Dr. Rebecca Jackson for the enlightening and motivating discussions that contributed to this research. We gratefully acknowledge the anonymous reviewers for their constructive contributions. This material is based upon work supported by the National Science Foundation Graduate Research Fellowship under Grant No. 2137420. C.R.M. was supported by the Army Research Office (Grant No. 78811EG).

Research conceptualization involved B.A.J. and C.R.M. Design of laboratory experiments was performed by A.L.M. and B.A.J. Collection and processing of experimental data was completed by A.L.M. Analysis of experimental data was primarily performed by A.L.M. with the support of B.A.J. and C.R.M. Analytical melt analysis was completed by C.R.M. The paper was written by A.L.M. with input from C.R.M. and B.A.J. All authors contributed comments and edits on the final draft.

[1] J. Mouginot, E. Rignot, A. A. Bjørk, M. van den Broeke, R. Millan, M. Morlighem, B. Noël, B. Scheuchl, and M. Wood, Forty-six years of Greenland Ice Sheet mass balance from 1972 to 2018, Proc. Natl. Acad. Sci. USA **116**, 9239 (2019).

[2] A. Shepherd *et al.*, A reconciled estimate of ice-sheet mass balance, Science **338**, 1183 (2012).

[3] D. Reidmiller, C. Avery, D. Easterling, K. Kunkel, K. Lewis, T. Maycock, and B. Stewart, *Impacts, Risks, and Adaptation in the United States: Fourth National Climate Assessment* (US Global Change Research Program, Washington, DC, USA, 2018), Vol. II.

[4] E. M. Enderlin, I. M. Howat, S. Jeong, M. J. Noh, J. H. van Angelen, and M. R. van den Broeke, An improved mass budget for the Greenland ice sheet, Geophys. Res. Lett. **41**, 866 (2014).

[5] R. H. Jackson, J. D. Nash, C. Kienholz, D. A. Sutherland, J. M. Amundson, R. J. Motyka, D. Winters, E. Skyllingstad, and E. C. Pettit, Meltwater intrusions reveal mechanisms for rapid submarine melt at a tidewater glacier, Geophys. Res. Lett. **47**, e2019GL085335 (2020).

[6] D. A. Sutherland, R. H. Jackson, C. Kienholz, J. M. Amundson, W. P. Dryer, D. Duncan, E. F. Eidam, R. J. Motyka, and J. D. Nash, Direct observations of submarine melt and subsurface geometry at a tidewater glacier, Science **365**, 369 (2019).

[7] D. Slater, F. Straneo, S. Das, C. Richards, T. Wagner, and P. Nienow, Localized plumes drive front-wide ocean melting of a Greenlandic tidewater glacier, Geophys. Res. Lett. **45**, 12350 (2018).

[8] E. De Andres, D. A. Slater, F. Straneo, J. Otero, S. Das, and F. Navarro, Surface emergence of glacial plumes determined by fjord stratification, Cryosphere **14**, 1951 (2020).

[9] K. Schild, R. Hawley, and B. Morriss, Subglacial hydrology at Rink Isbræ, West Greenland inferred from sediment plume appearance, Ann. Glaciol. **57**, 118 (2016).

[10] S. Kimura, P. R. Holland, A. Jenkins, and M. Piggott, The effect of meltwater plumes on the melting of a vertical glacier face, J. Phys. Oceanogr. **44**, 3099 (2014).

[11] K. D. Mankoff, F. Straneo, C. Cenedese, S. B. Das, C. G. Richards, and H. Singh, Structure and dynamics of a subglacial discharge plume in a Greenlandic fjord, J. Geophys. Res.: Oceans **121**, 8670 (2016).

[12] A. Jenkins, K. W. Nicholls, and H. F. J. Corr, Observation and parameterization of ablation at the base of Ronne ice shelf, Antarctica, J. Phys. Oceanogr. **40**, 2298 (2010).
[13] M. G. McPhee, G. A. Maykut, and J. H. Morison, Dynamics and thermodynamics of the ice/upper ocean system in the marginal ice zone of the Greenland sea, J. Geophys. Res.: Oceans **92**, 7017 (1987).
[14] A. Jenkins, Convection-driven melting near the grounding lines of ice shelves and tidewater glaciers, J. Phys. Oceanogr. **41**, 2279 (2011).
[15] S. J. Magorrian and A. Wells, Turbulent plumes from a glacier terminus melting in a stratified ocean, J. Geophys. Res.: Oceans **121**, 4670 (2016).
[16] K. Schulz, A. Nguyen, and H. Pillar, An improved and observationally-constrained melt rate parameterization for vertical ice fronts of marine terminating glaciers, Geophys. Res. Lett. **49**, e2022GL100654 (2022).
[17] R. Sciascia, F. Straneo, C. Cenedese, and P. Heimbach, Seasonal variability of submarine melt rate and circulation in an East Greenland fjord, J. Geophys. Res.: Oceans **118**, 2492 (2013).
[18] A. L. McCutchan and B. A. Johnson, Laboratory experiments on ice melting: A need for understanding dynamics at the ice-water interface, J. Mar. Sci. Eng. **10**, 1008 (2022).
[19] J. M. Dumoré, H. J. Merk, and J. A. Prins, Heat transfer from water to ice by thermal convection, Nature (London) **172**, 460 (1953).
[20] J. Schenk and F. A. M. Schenkels, Thermal free convection from an ice sphere in water, Appl. Sci. Res. **19**, 465 (1968).
[21] C. R. Vanier and C. Tien, Free convection melting of ice spheres, AIChE J. **16**, 76 (1970).
[22] M. S. Bendell and B. Gebhart, Heat transfer and ice-melting in ambient water near its density extremum, Int. J. Heat Mass Transfer **19**, 1081 (1976).
[23] C. R. Dutton and A. M. Sharan, A study of the heat transfer process in fresh water at low temperatures, Cold Reg. Sci. Technol. **15**, 13 (1988).
[24] B. Gebhart and T. Wang, An experimental study of melting vertical ice cylinders in cold water, Chem. Eng. Commun. **13**, 197 (1982).
[25] S. Weady, J. Tong, A. Zidovska, and L. Ristroph, Anomalous convective flows carve pinnacles and scallops in melting ice, Phys. Rev. Lett. **128**, 044502 (2022).
[26] N. W. Wilson and B. D. Vyas, Velocity profiles near a vertical ice surface melting into fresh water, J. Heat Transfer **101**, 313 (1979).
[27] V. P. Carey and B. Gebhart, Visualization of the flow adjacent to a vertical ice surface melting in cold pure water, J. Fluid Mech. **107**, 37 (1981).
[28] K. Eijpen, C. R. Warren, and D. I. Benn, Subaqueous melt rates at calving termini: A laboratory approach, Ann. Glaciol. **36**, 179 (2003).
[29] E. G. Josberger and S. Martin, A laboratory and theoretical study of the boundary layer adjacent to a vertical melting ice wall in salt water, J. Fluid Mech. **111**, 439 (1981).
[30] R. C. Kerr and C. D. McConnochie, Dissolution of a vertical solid surface by turbulent compositional convection, J. Fluid Mech. **765**, 211 (2015).
[31] C. D. McConnochie and R. C. Kerr, Dissolution of a sloping solid surface by turbulent compositional convection, J. Fluid Mech. **846**, 563 (2018).
[32] H. E. Huppert and E. G. Josberger, The melting of ice in cold stratified water, J. Phys. Oceanogr. **10**, 953 (1980).
[33] H. E. Huppert and J. S. Turner, Ice blocks melting into a salinity gradient, J. Fluid Mech. **100**, 367 (1980).
[34] C. D. McConnochie and R. C. Kerr, The effect of a salinity gradient on the dissolution of a vertical ice face, J. Fluid Mech. **791**, 589 (2016).
[35] Y. L. Hao and Y. X. Tao, Heat transfer characteristics of melting ice spheres under forced and mixed convection, J. Heat Transfer **124**, 891 (2002).
[36] C. Cenedese and V. M. Gatto, Impact of a localized source of subglacial discharge on the heat flux and submarine melting of a tidewater glacier: A laboratory study, J. Phys. Oceanogr. **46**, 3155 (2016).
[37] C. Cenedese and V. M. Gatto, Impact of two plumes' interaction on submarine melting of tidewater glaciers: A laboratory study, J. Phys. Oceanogr. **46**, 361 (2016).

[38] C. McConnochie and R. Kerr, Enhanced ablation of a vertical ice wall due to an external freshwater plume, Geophys. Res. Lett. **810**, 429 (2017).
[39] R. Sciascia, C. Cenedese, D. Nicolì, P. Heimbach, and F. Straneo, Impact of periodic intermediary flows on submarine melting of a Greenland glacier, J. Geophys. Res.: Oceans **119**, 7078 (2014).
[40] A. FitzMaurice, C. Cenedese, and F. Straneo, Nonlinear response of iceberg side melting to ocean currents, Geophys. Res. Lett. **44**, 5637 (2017).
[41] A. FitzMaurice, C. Cenedese, and F. Straneo, A laboratory study of iceberg side melting in vertically sheared flows, J. Phys. Oceanogr. **48**, 1367 (2018).
[42] E. W. Hester, C. D. McConnochie, C. Cenedese, L. A. Couston, and G. Vasil, Aspect ratio affects iceberg melting, Phys. Rev. Fluids **6**, 023802 (2021).
[43] M. Bushuk, D. M. Holland, T. P. Stanton, A. Stern, and C. Gray, Ice scallops: A laboratory investigation of the ice–water interface, J. Fluid Mech. **873**, 942 (2019).
[44] E. Ramudu, B. Hirsh, P. Olson, and A. Gnanadesikan, Turbulent heat exchange between water and ice at an evolving ice-water interface, J. Fluid Mech. **798**, 572 (2016).
[45] N. Machicoane, J. Bonaventure, and R. Volk, Melting dynamics of large ice balls in a turbulent swirling flow, Phys. Fluids **25**, 125101 (2013).
[46] H. Stapountzis, T. G. Dimitriadis, K. Giourgas, and K. Kotsanidis, Melting of ice spheres in nearly isotropic turbulence with zero mean, *Proceedings of the 10th Pacific Symposium on Flow Visualization and Image Processing* (Naples, Italy, 2015).
[47] M. S. Davies Wykes, J. M. Huang, G. A. Hajjar, and L. Ristroph, Self-sculpting of a dissolvable body due to gravitational convection, Phys. Rev. Fluids **3**, 043801 (2018).
[48] S. Bounoua, G. Bouchet, and G. Verhille, Tumbling of inertial fibers in turbulence, Phys. Rev. Lett. **121**, 124502 (2018).
[49] C. Goepfert, J. L. Marié, D. Chareyron, and M. Lance, Characterization of a system generating a homogeneous isotropic turbulence field by free synthetic jets, Exp. Fluids **48**, 809 (2010).
[50] W. Hwang and J. Eaton, Creating homogeneous and isotropic turbulence without a mean flow, Exp. Fluids **36**, 444 (2004).
[51] E. Variano, E. Bodenschatz, and E. Cowen, A random synthetic jet array driven turbulence tank, Exp. Fluids **37**, 613 (2004).
[52] D. R. Webster, A. Brathwaite, and J. Yen, A novel laboratory apparatus for simulating isotropic oceanic turbulence at low Reynolds number, Limnol. Oceanogr. Methods **2**, 1 (2004).
[53] A. Ghazi Nezami, M. Byron, and B. A. Johnson, Laboratory generation of zero mean flow homogeneous isotropic turbulence: Non-grid approaches, Flow **3**, E42 (2023).
[54] A. L. McCutchan and B. A. Johnson, An experimental apparatus for generating homogeneous isotropic turbulence, Exp. Fluids **64**, 177 (2023).
[55] E. Variano and E. Cowen, A random-jet-stirred turbulence tank, J. Fluid Mech. **604**, 1 (2008).
[56] B. A. Johnson and E. A. Cowen, Turbulent boundary layers absent mean shear, J. Fluid Mech. **835**, 217 (2018).
[57] R. J. Adrian, Particle-image techniques for experimental fluid mechanics, Annu. Rev. Fluid Mech. **23**, 261 (1991).
[58] W. Thielicke and E. J. Stamhuis, PIVlab – Towards user-friendly, affordable and accurate digital particle image velocimetry in MATLAB, J. Open Res. Software **2**, e30 (2014).
[59] W. Thielicke and E. J. Stamhuis, PIVlab - TIME-resolved digital particle image velocimetry tool for MATLAB, version 2.02, 2019.
[60] E. Cowen and S. Monismith, A hybrid digital particle tracking velocimetry technique, Exp. Fluids **22**, 199 (1997).
[61] I. Reba, Applications of the Coanda effect, Sci. Am. **214**, 84 (1966).
[62] P. Mcleod, D. S. Riley, and R. S. J. Sparks, Melting of a sphere in hot fluid, J. Fluid Mech. **327**, 393 (1996).
[63] C. Cohen, M. Berhanu, J. Derr, and S. Courrech du Pont, Buoyancy-driven dissolution of inclined blocks: Erosion rate and pattern formation, Phys. Rev. Fluids **5**, 053802 (2020).

[64] M. Moore, L. Ristroph, S. Childress, J. Zhang, and M. Shelley, Self-similar evolution of a body eroding in a fluid flow, Phys. Fluids **25**, 116602 (2013).
[65] V. Levich and C. Tobias, Physicochemical hydrodynamics, J. Electrochem. Soc. **110**, 251C (1963).
[66] P. Doron, L. Bertuccioli, J. Katz, and T. R. Osborn, Turbulence characteristics and dissipation estimates in the coastal ocean bottom boundary layer from PIV data, J. Phys. Oceanogr. **31**, 2108 (2001).
[67] Y. H. Pao, Structure of turbulent velocity and scalar fields at large wavenumbers, Phys. Fluids **8**, 1063 (1965).
[68] S. B. Pope, *Turbulent Flows* (Cambridge University Press, Cambridge, UK, 2000).
[69] S. A. Talke, A. R. Horner-Devine, C. C. Chickadel, and A. T. Jessup, Turbulent kinetic energy and coherent structures in a tidal river, J. Geophys. Res.: Oceans **118**, 6965 (2013).
[70] I. Fer, Scaling turbulent dissipation in an Arctic fjord, Ocean Mixing **53**, 77 (2006).
[71] I. Fer, Z. Koenig, I. E. Kozlov, M. Ostrowski, T. P. Rippeth, L. Padman, A. Bosse, and E. Kolås, Tidally forced lee waves drive turbulent mixing along the Arctic Ocean margins, Geophys. Res. Lett. **47**, e2020GL088083 (2020).
[72] M. G. McPhee and T. P. Stanton, Turbulence in the statically unstable oceanic boundary layer under Arctic leads, J. Geophys. Res.: Oceans **101**, 6409 (1996).
[73] B. Scheifele, S. Waterman, L. Merckelbach, and J. R. Carpenter, Measuring the dissipation rate of turbulent kinetic energy in strongly stratified, low-energy environments: A case study from the Arctic Ocean, J. Geophys. Res.: Oceans **123**, 5459 (2018).
[74] B. Scheifele, S. Waterman, and J. R. Carpenter, Turbulence and mixing in the Arctic Ocean's Amundsen Gulf, J. Phys. Oceanogr. **51**, 169 (2021).
[75] T. Oehmke and E. Variano, A new particle for measuring mass transfer in turbulence, Exp. Fluids **62**, 16 (2021).
[76] A. Hixson and J. Crowell, Dependence of reaching velocity upon surface and agitation, Ind. Eng. Chem. **23**, 923 (1931).